




Article

Dielectric Studies of Bi₂MoO₆/Graphene Oxide and La-Doped Bi₂MoO₆/Graphene Oxide Nanocomposites

Syed Farooq Adil ^{1,*}, Shoomaila Latif ², Muhammad Waqar ³, Muhammad Imran ^{3,*}, Sadia Noreen ³, Mujeeb Khan ¹, Mohammed Rafi Shaik ¹ and Mohammad Rafe Hatshan ¹

¹ Department of Chemistry, College of Science, King Saud University, P.O. Box 2455, Riyadh 11451, Saudi Arabia; kmujeeb@ksu.edu.sa (M.K.); mrshaik@ksu.edu.sa (M.R.S.); mhatshan@ksu.edu.sa (M.R.H.)

² School of Physical Sciences, University of the Punjab, Lahore 54590, Pakistan; shoomaila.sps@pu.edu.pk

³ Institute of Chemistry, University of the Punjab, Lahore 54590, Pakistan; waqar0100@gmail.com (M.W.); sadian543@gmail.com (S.N.)

* Correspondence: sfadil@ksu.edu.sa (S.F.A.); imran.hons@pu.edu.pk (M.I.); Tel.: +966-11-4670439 (S.F.A.)

Abstract: The mixed metal oxides Bi₂MoO₆ and La-doped Bi₂MoO₆ were prepared by the sol–gel method. Then, varying quantities of the as-prepared mixed metal oxides were blended with graphene oxide (GO), employing sonication, to obtain Bi₂MoO₆/GO (BM/GO) and La-Bi₂MoO₆/GO (LBM/GO) nanocomposites. These prepared materials were characterized by different techniques such as thermal gravimetric analysis (TGA), X-ray diffraction (XRD), Brunauer-Emmett-Teller (BET), X-ray photoelectron spectroscopy (XPS), scanning electron microscope (SEM), and transmission electron microscopy (TEM). Dielectric properties were studied by using a precision impedance analyzer. Dielectric constant and loss tan of the synthesized composites were studied as a function of frequency by using a precision impedance analyzer. Overall, the dielectric constant (ϵ') observed for the LBM/GO composites was higher than that of BM/GO.

Keywords: dielectric studies; Bi₂MoO₆; lanthanum; graphene oxide



Citation: Adil, S.F.; Latif, S.; Waqar, M.; Imran, M.; Noreen, S.; Khan, M.; Shaik, M.R.; Hatshan, M.R. Dielectric Studies of Bi₂MoO₆/Graphene Oxide and La-Doped Bi₂MoO₆/Graphene Oxide Nanocomposites. *Metals* **2021**, *11*, 559. <https://doi.org/10.3390/met11040559>

Received: 18 February 2021

Accepted: 26 March 2021

Published: 29 March 2021

Publisher's Note: MDPI stays neutral with regard to jurisdictional claims in published maps and institutional affiliations.



Copyright: © 2021 by the authors. Licensee MDPI, Basel, Switzerland. This article is an open access article distributed under the terms and conditions of the Creative Commons Attribution (CC BY) license (<https://creativecommons.org/licenses/by/4.0/>).

1. Introduction

A growing demand for electric charge storage devices, due to the invention of battery-powered automobiles and other devices, has led to the study of the preparation of materials with enhanced dielectric properties. A variety of nanocomposites such as Mn-substituted ZnFe₂O₄; Co₂Y hexaferrites substituted by Mn-Ge, Ce-Nd₂Zr₂O₇, Co(II), Ni(II), Cu(II), and Mn(II)-oxaloyldihydrazone complexes; and ZnO microspheres with polyaniline (PANI) have been studied for their dielectric behaviors due to the fact that nanocomposites possess unique properties as compared to bulk material [1–3]. Nanocomposites have great importance due to their remarkable catalytic, dielectric, and luminescence properties, based on the morphology of the nanomaterials. The electrical conductance and thermal stability of the metal nanocomposites can be improved by the help of a carbon-based support, usually achieved with graphene oxides [4,5].

One such carbon-based support is graphene, a 2D Material that has been found to be an excellent support for the enhancement of properties of the resulting nanocomposites [6–13]. Various reports of the use of graphene can be found in the literature, such as poly(p-phenylene benzobisoxazole/graphene, PVA/graphene composites graphene oxide (GO)/Zn_xFe_{1-x}Fe₂O₄ composites, graphene/BaTiO nanocomposites rGO-Cu₂O, etc., for the creation of nanocomposites that display enhanced dielectric properties due to the inclusion of graphene [14–16].

Furthermore, the incorporation of metals and non-metals with metal oxides nanoparticles also enhances the functionality of the materials. One such metal that has been extensively studied is bismuth, and there are a series of nanocomposites (Bi₂WO₆, BaTiO₃Bi₂O₃,

Bi_2S_3 , BiVO_4 , $\text{Bi}_2\text{Ti}_2\text{O}_7$, $\text{Bi}_{12}\text{TiO}_{20}$ and $\text{Bi}_2\text{InNbO}_7$) that show a variety of properties [17–21]. Bismuth molybdate (Bi_2MoO_6) is a versatile metal molybdate with photoelectric characteristics that has been widely used as a photocatalyst and as an anode material in lithium batteries. Some notable citations in this regard are available in the literature [22–26].

Recently, bismuth molybdate (Bi_2MoO_6) was employed as a photocatalyst, exhibiting increased performance among metal molybdates for the degradation of dyes and luminescence, and it has been synthesized by various methods: co-precipitation, hydrothermal, solid state reaction, and sol–gel [27]. In continuation of our efforts to prepare various graphene-based nanocomposites, we extended our previous work regarding synthesis and morphological studies of Bi_2MoO_6 and La-doped Bi_2MoO_6 [28–30], and herein we report on the graphene oxide nanocomposites of Bi_2MoO_6 and La-doped Bi_2MoO_6 , i.e., $\text{Bi}_2\text{MoO}_6/\text{GO}$ and La- $\text{Bi}_2\text{MoO}_6/\text{GO}$ composites, respectively, and their dielectric behavior.

2. Materials and Methods

2.1. Materials

All chemicals used for the synthesis, such as graphite powder, sodium molybdate ($\text{Na}_2\text{Mo}_2\text{O}_4 \times 2\text{H}_2\text{O}$), bismuth chloride (BiCl_3), and lanthanum chloride ($\text{LaCl}_3 \times 7\text{H}_2\text{O}$), were of analytical grade purchased from Sigma Aldrich and PubChem (Saint Louis, MO, USA). Bi_2MoO_6 and La-doped Bi_2MoO_6 were synthesized using a previously reported method [28].

2.2. Methods

Graphene oxide was synthesized by the modified Hummers method [31]. A variety of nanocomposites of bismuth molybdate and lanthanum-doped bismuth molybdate with graphene oxide were synthesized by depositing varying amounts by weight of Bi_2MoO_6 and La- Bi_2MoO_6 on graphene oxide to yield 2, 3, and 4% of $\text{Bi}_2\text{MoO}_6/\text{GO}$ (BM/GO) and La- $\text{Bi}_2\text{MoO}_6/\text{GO}$ (LBM/GO). The mixed metal oxides and graphene oxide were dispersed in deionized water by applying sonication for 3 h. After sonication, the samples were dried in an electric oven at 90 °C for 48 h, and we obtained X% BM/GO (X wt.% $\text{Bi}_2\text{MoO}_6/\text{GO}$) and X% LBM/GO (X wt.% La- $\text{Bi}_2\text{MoO}_6/\text{GO}$) composites, where X = 2, 3, or 4, which denotes the wt.% of the mixed metal oxide in the GO nanocomposite.

2.3. Characterization

The crystalline structures of the as synthesized nanocomposites were characterized with XRD patterns on a Bruker D2 Phaser X-ray diffractometer with Cu K α radiation ($\lambda = 1.5418 \text{ \AA}$), having accelerating voltage and current of 30 kV and 10 mA, respectively (Bruker, Berlin, Germany). TGA was performed by heating the samples in an N_2 flow using a Perkin-Elmer Thermogravimetric Analyzer 7 with a heating rate of 10 °C/min (Perkin-Elmer, Waltham, MA, USA). BET surface area and BJH pore volume were measured by an N_2 adsorption-desorption isotherm with a liquid nitrogen temperature of $-196 \text{ }^\circ\text{C}$ using Micromeritics (Gemini VII, 2390 surface area and porosity, Norcross, GA, USA). The samples were degassed at 120 °C for 3 h using N_2 gas. The surface morphology of the nanocomposites was determined by scanning electron microscopy (SEM, Jeol, JED-2200 series, Tokyo, Japan). Transmission electron microscopy (TEM) analysis of nanocomposite measurements was carried out using Jeol TEM model JEM-1011 (Jeol, Tokyo, Japan) at 100 keV. XPS spectra were measured on a PHI 5600 Multi-Technique XPS (Physical Electronics, Lake Drive East, Chanhassen, MN, USA) using monochromatized Al K α at 1486.6 eV.

3. Results and Discussions

3.1. Thermal Gravimetric Analysis

A thermal gravimetric analysis (TGA, Perkin-Elmer, Waltham, MA, USA) was conducted to identify the thermal behavior of all the synthesized composites. The results of 4% BM/GO and 4% LBM/GO are compared in Figure 1, while the TGA curves of other

compositions are given in the supplementary data (Figure S1). Among these composites, in general, a large weight loss was observed between 220 and 445 °C, which can be attributed to the thermal decomposition of rGO in these composites. Such a large loss is in agreement with similar degradation patterns of $\text{Bi}_2\text{MoO}_6/\text{rGO}$ composites [22]. The TGA thermogram of Bi_2MoO_6 reveals that there was an 8% weight loss and that of $\text{La-Bi}_2\text{MoO}_6$ shows a weight loss of up to 16%, indicating that the later nanocomposite is thermally less stable than its precursor. However, when the GO nanocomposites of the mixed metal oxides BM and LBM, i.e., $X\% \text{Bi}_2\text{MoO}_6/\text{GO}$ and $X\% \text{La-Bi}_2\text{MoO}_6/\text{GO}$, were subjected to similar studies wherein the samples were heated up to 800 °C starting from 25 °C at a heating rate of 10 °C/min under an inert atmosphere, a similar trend of thermal stability was observed, indicating the formation of composites. However, when the La-doped Bi_2MoO_6 was subjected to a similar study, it was found that the weight loss was up to 16%, indicating that the later nanocomposite, i.e., 4% LBM/GO, is thermally less stable.

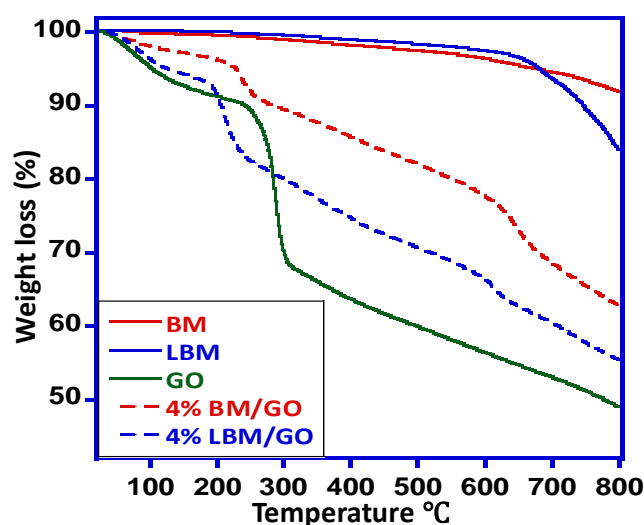


Figure 1. Comparative thermal degradation patterns of Bi_2MoO_6 (BM), $\text{La-Bi}_2\text{MoO}_6$ (LBM), graphene oxide (GO), 4% BM/GO, and 4% LBM/GO.

3.2. X-ray Diffraction

The XRD pattern of the prepared 4% BM/GO and 4% LBM/GO composites is given in Figure 2. The diffractogram obtained for the sample of 4% BM/GO revealed the presence of GO along with the pattern of Bi_2MoO_6 (JCPDS No. 76-2388), which yielded diffraction peaks at 2θ values 23.5° (111), 28.2° (131), 32.5° (002), 33.2° (060), 36.1° (151), 46.8° (202), 47.2° (260), 55.5° (133), 56.4° (191), and 58.4° (262) that were found in the original mixed metal oxide BM [32]. However, the XRD pattern of 4% LBM/GO revealed the presence of mixed phases of $\text{La}_2\text{Mo}_2\text{O}_9$ and Bi_2MoO_6 along with GO [32–34].

3.3. BET Analysis

The nitrogen adsorption isotherms of 4% BM/GO and 4% LBM/GO composites measured at 333K are shown in Figure 3. From the isotherms obtained, it can be observed that the adsorption of N_2 was much higher in the composites than in their precursors, suggesting that the enormous alteration of structural characteristics takes place due to incorporation of GO in the system [35]. Moreover, the surface area of the 4% BM/GO and 4% LBM/GO composites was found to be 12 m^2/g and 10.7 m^2/g , respectively, which is several times greater than that of the precursors Bi_2MoO_6 (1.0277 m^2/g) and La-doped Bi_2MoO_6 (3.4077 m^2/g), respectively [28]. This difference in surface area can also be attributed to the GO incorporation with BM and LBM precursors [36].

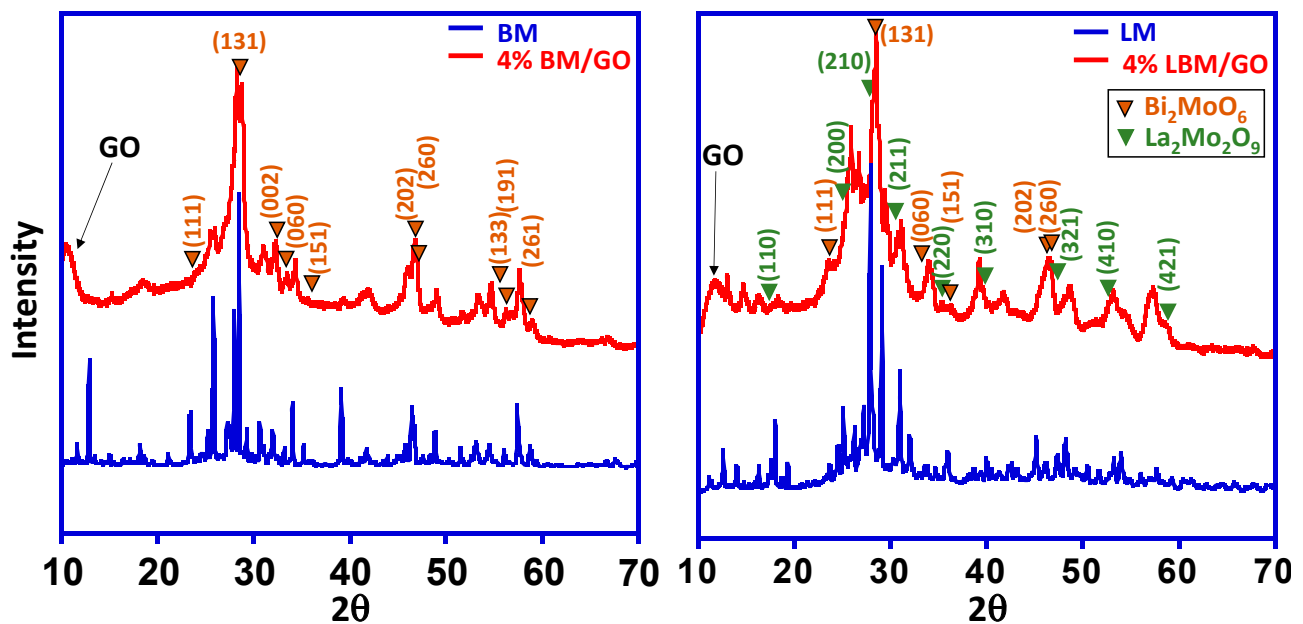


Figure 2. Comparative XRD patterns of BM, 4% BM/GO, and LBM, 4% LBM/GO composites.

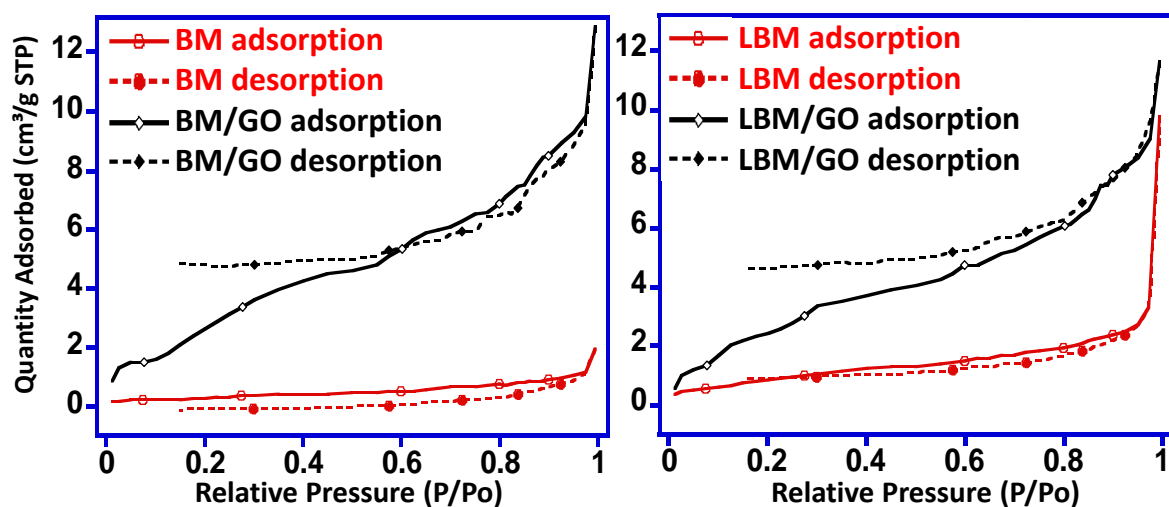


Figure 3. Nitrogen adsorption isotherms of 4% BM/GO and 4% LBM/GO composites.

Furthermore, when comparing the pore distribution of the composites with the precursor metal oxides, i.e., BM and LBM, it was observed that the pore size of the composites ranged from 1.1 to $18.6 \times 10^{-3} \text{ cm}^3/\text{g}$ and 2.8 to $19.7 \times 10^{-3} \text{ cm}^3/\text{g}$ for the 4% BM/GO and 4% LBM/GO composites, respectively (Figure 4).

3.4. Microscopic Analysis

The surface morphology of the prepared 4% BM/GO and 4% LBM/GO composites was examined by SEM, and the respective SEM micrograms are shown in Figure 5. The surface morphology of 4% BM/GO possesses irregular shining particles with small crystals of bismuth molybdate on a graphene oxide platform. The surface morphology of 4% LBM/GO exhibits a distribution of particles arranged as relatively large rod-like crystals of lanthanum molybdate embedded on a graphene oxide platform. The surface morphology of both composites is quite different than that of Bi_2MoO_6 and $\text{La-Bi}_2\text{MoO}_6$, which are dense rod-like and scattered granular, respectively [28].

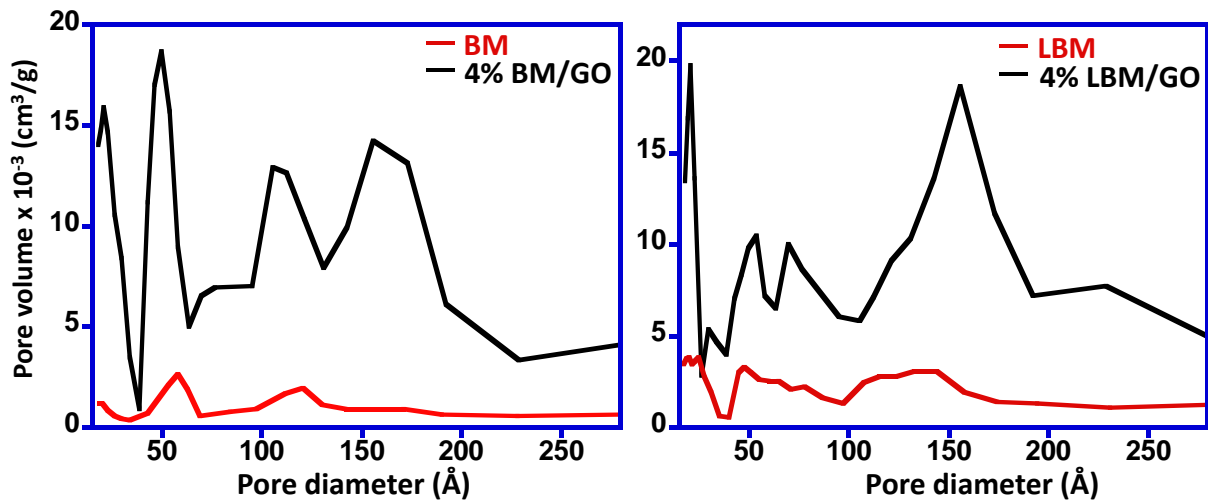


Figure 4. Pore distribution curves of 4% BM/GO and 4% LBM/GO composites.

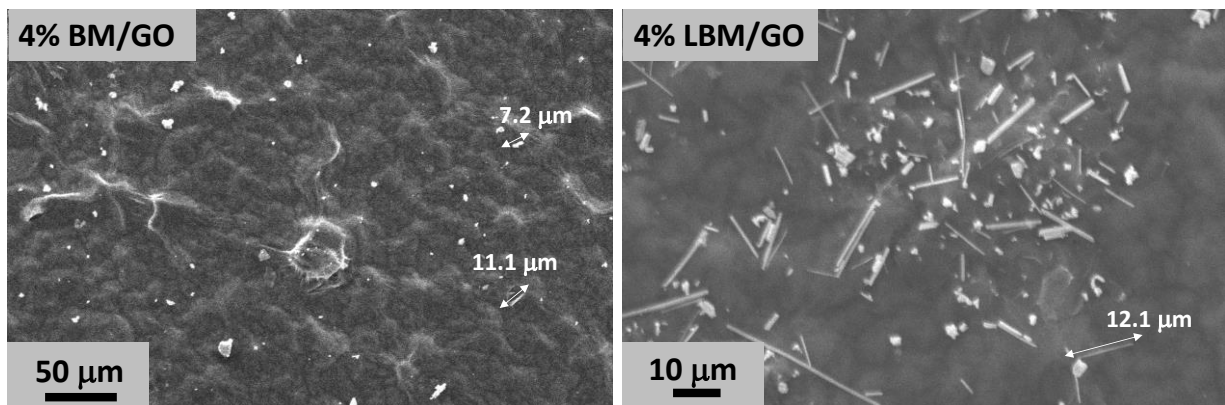


Figure 5. Scanning electron micrograms of 4% BM/GO and 4% LBM/GO composites.

The prepared composites were subjected to TEM analysis by dispersing the prepared composites in hexane and using a sonicator water bath, then, the dispersed solution was dropped on the TEM grid to evaluate the dispersion of BM and LBM on the graphene oxide sheets. It was observed that the dispersion of LBM, i.e., La-Bi₂MoO₆, on the graphene oxide sheets in the composite 4% LBM/GO was superior to that observed in the case of BM, i.e., Bi₂MoO₆ in the 4% BM/GO composite, wherein agglomeration of the mixed metal oxides was seen on the surface of the GO. The TEM images obtained for both the composites, i.e., 4% BM/GO and 4% LBM/GO, are given in Figure 6.

3.5. X-ray Photoelectron Spectroscopy

X-ray photoelectron spectroscopy is one of the best tools to analyze the surface composition and particularly the valence state of elements in these composites. The scan of the 4% LBM/GO composite revealed the presence of Bi, Mo, O, and La elements in the prepared composites, and an additional signal corresponding to the element C revealed the successful doping of GO in the nanocomposite (Figure 7). The full spectrum for the 4% LBM/GO composite contains peaks for C 1s (287 eV), O 1s (537 eV), Mo 3d (235 eV), Bi 4f (158 eV), and La 3d. These results are in agreement with previous literature [22,28]. It was observed that there was no change in the binding energies of the respective elements of the mixed metal oxides, indicating that the formation of the composites is by physisorption of the mixed metal oxides, i.e., BM and LBM, on the surface of the employed GO, as confirmed by the TEM images.

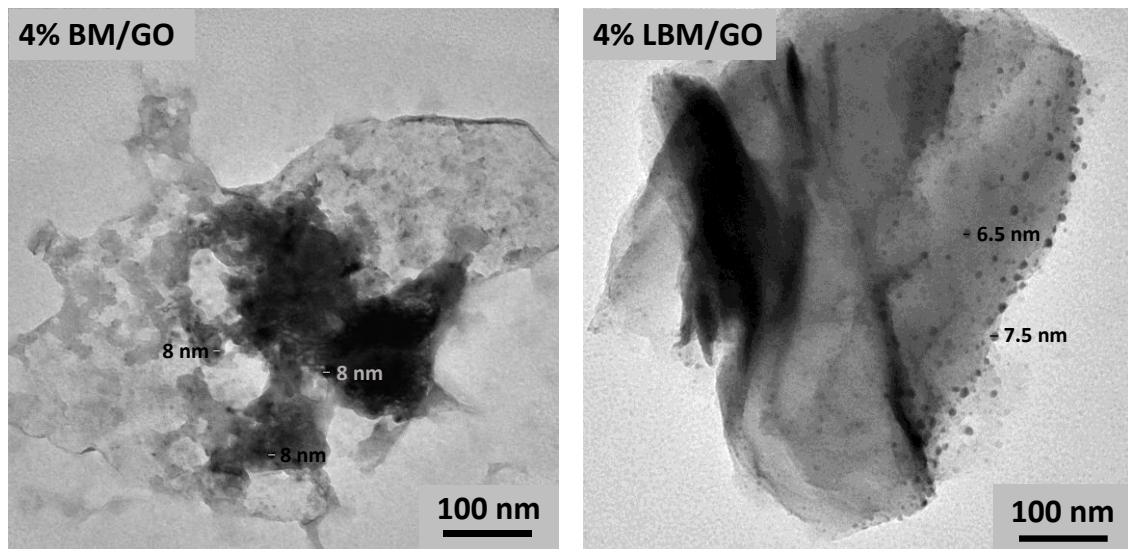


Figure 6. Transmission electron microscopy analysis of 4% BM/GO and 4% LBM/GO composites.

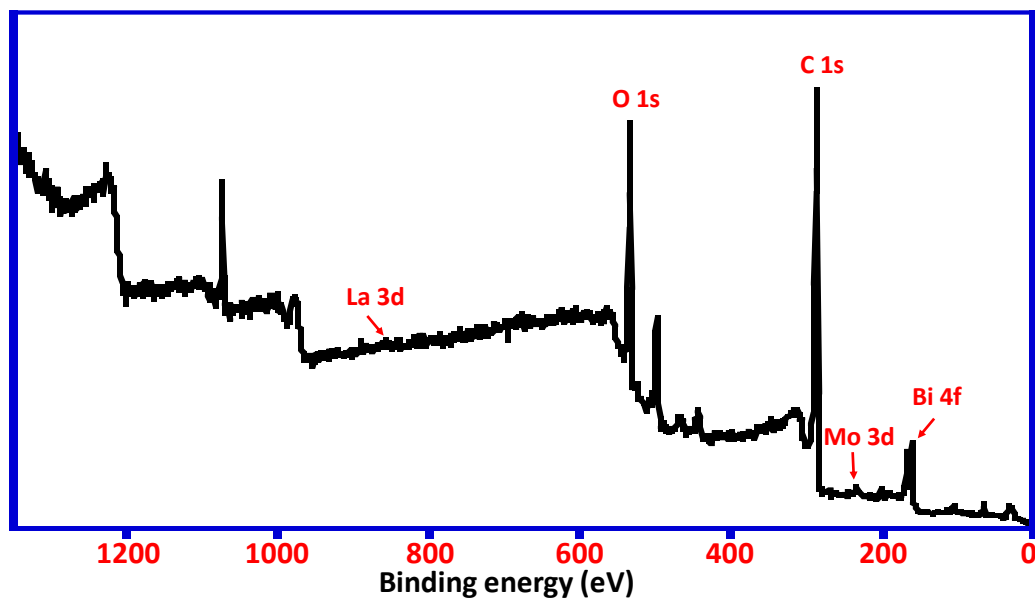


Figure 7. XPS spectra of the 4% LBM/GO composite.

3.6. Dielectric Properties

Dielectric properties of $\text{Bi}_2\text{MoO}_6/\text{GO}$ and $\text{La-Bi}_2\text{MoO}_6/\text{GO}$ as a function of frequency were studied by using an impedance analyzer, and the values of the dielectric constants were plotted against the log of frequency, as shown in Figure 8a,b and Figure 9a,b. Figure 8a,b shows the increase in dielectric constant from X% BM/GO ($X = 2, 3,$ and 4). ϵ' decreases with an increase in frequency. High dielectric constants at low frequencies were attributed to the electrode polarization phenomenon, wherein an increase in of the electrode potential lags behind the frequency, and space charges have less time to be arranged according to the applied electric field [37]. An increase in ϵ' was observed with an increase in BM content from 2 to 4% in the GO nanocomposite. Values of ϵ' were 17.69, 76.67, and 142.33 for 2, 3 and 4%, respectively. A high dielectric constant was considered due to the electronic and ionic polarizability, and contribution by the oxide contents and Bi ions mainly contributed to the high ϵ' [38,39]. Moreover, existence of the oxygenated groups in the GO caused entrapment of Bi ions and reduced the interaction of Bi with

molybdate ions, and hence, more available Bi caused a high ϵ' [40]. ϵ' observed for the LBM/GO composites was higher than that of the undoped nanocomposite, i.e., BM/GO, but overall, the value of the ϵ' was much lower than that of $\text{Bi}_2\text{MoO}_6/\text{GO}$. Values observed for the ϵ' of $\text{La-Bi}_2\text{MoO}_6/\text{GO}$, which were 43.9, 48.89, and 51.28 for 2, 3, and 4% weight of $\text{La-Bi}_2\text{MoO}_6$, dispersed in a fixed amount of GO. The low ϵ' was attributed to the increased conductivity of the oxide ions in $\text{La-doped Bi}_2\text{MoO}_6$ [41].

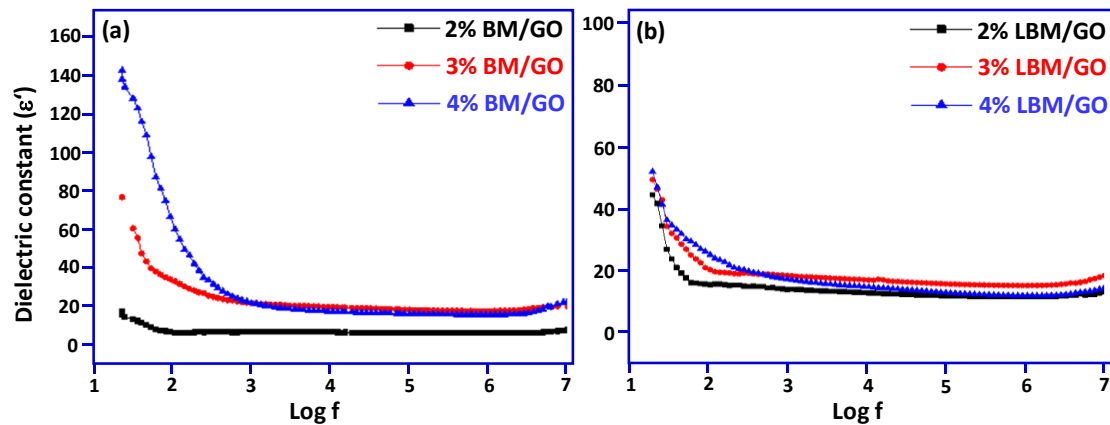


Figure 8. (a): Comparative graphs between the dielectric constant (ϵ') and $\log f$ for composites X% BM/GO (X = 2, 3, and 4) (b) X% LBM/GO (X = 2, 3, and 4).

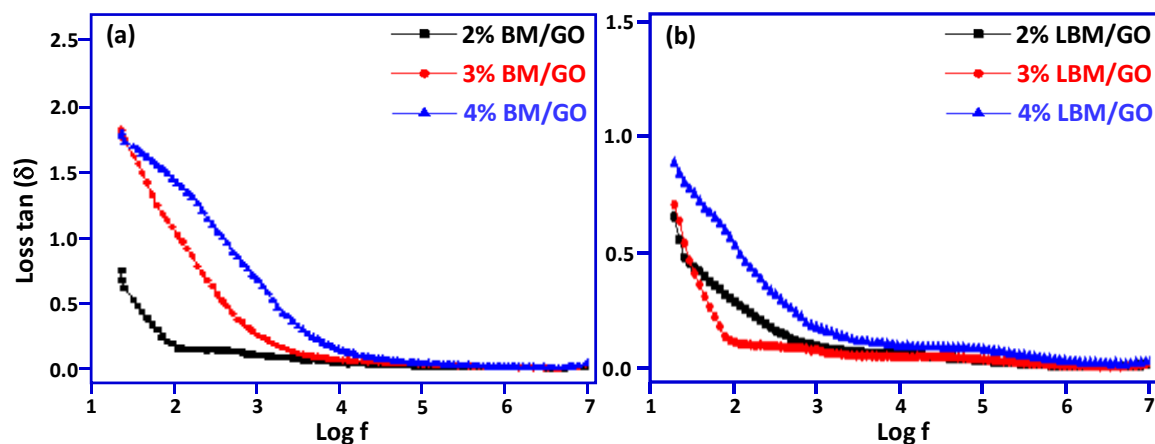


Figure 9. (a): Comparative graphs between $\tan \delta$ and $\log f$ for composites X% BM/GO (X = 2, 3, and 4) (b) X% LBM/GO (X = 2, 3, and 4).

The loss tangents ($\tan \delta$) for $\text{Bi}_2\text{MoO}_6/\text{GO}$ and $\text{La-Bi}_2\text{MoO}_6/\text{GO}$ plotted against frequency, as shown in Figure 9a,b, show a similar behavior as that of ϵ' . Values of $\tan \delta$ were 0.75, 1.82, and 1.79 for 2, 3, and 4% weight of Bi_2MoO_6 , respectively, and the values of $\tan \delta$ of $\text{La-Bi}_2\text{MoO}_6/\text{GO}$ were 0.65, 0.71, and 0.88, respectively. The increase in $\tan \delta$ with the increase in Bi_2MoO_6 content in GO is attributed to the conductive nature of Bi_2MoO_6 [42], while the increase in $\tan \delta$ with increase in $\text{Bi}_2\text{MoO}_6/\text{GO}$ is attributed to the conductive network formation, dipole polarization, and interfacial polarization [43], as there exists a relation between electrical conduction ϵ' and ϵ'' [44,45].

4. Conclusions

Composites of $\text{GO}/\text{Bi}_2\text{MoO}_6$ and $\text{La-doped GO}/\text{Bi}_2\text{MoO}_6$ were synthesized by sonication. An increase in the dielectric constant with an increase in Bi_2MoO_6 content was observed with an ϵ' of 142.33 at 4 wt.% of Bi_2MoO_6 . A similar increasing trend was shown for $\text{La-doped Bi}_2\text{MoO}_6$, with an overall value of ϵ' 51.28. $\tan \delta$ was 1.79 and 0.88 for 4%

GO/Bi₂MoO₆ and La-doped GO/Bi₂MoO₆, respectively. Overall, the present work opens an avenue for the controlled synthesis of GO/Bi₂MoO₆ and La-doped GO/Bi₂MoO₆ and directs our attention to new roles of GO in the controllable synthesis of new materials for possible applications in capacitive and charge storage devices.

Supplementary Materials: The following are available online at <https://www.mdpi.com/article/10.3390/met11040559/s1>, Figure S1: Comparative thermal degradation patterns of (a) BM, LM, GO, 2% BM/GO, 3% BM/GO, 2% LBM/GO, and 3% BM/GO.

Author Contributions: Conceptualization, M.I. and S.F.A.; methodology, S.L., M.W., and S.F.A.; software, M.W.; validation, M.W. and S.F.A.; formal analysis, M.W., M.I., S.N., M.K., and M.R.S.; investigation, S.L., M.I., S.N., M.K., and M.R.S.; resources, M.I. and S.F.A.; data curation, S.L., M.I., S.N., M.K., and M.R.S.; writing—original draft preparation, M.W. and S.F.A.; writing—review and editing, M.W., S.F.A., M.K., and M.R.S.; visualization, M.R.H.; supervision, M.I., S.F.A., and M.R.H.; project administration, M.R.H.; funding acquisition, M.R.H. All authors have read and agreed to the published version of the manuscript.

Funding: The authors extend their appreciation to the Deputyship for Research & Innovation, “Ministry of Education” in Saudi Arabia for funding this research work through the project number IFKSURG-2020-142.

Institutional Review Board Statement: Not applicable.

Informed Consent Statement: Not applicable.

Data Availability Statement: Data are contained within the article or Supplementary material.

Acknowledgments: The authors extend their appreciation to the Deputyship for Research & Innovation, “Ministry of Education” in Saudi Arabia for funding this research work through the project number IFKSURG-2020-142.

Conflicts of Interest: The authors declare no conflict of interest.

References

- Huebner, E.U. (Ed.) *Nickel Alloys*; Marcel Dekker Inc.: New York, NY, USA; Basel, Switzerland, 2000; 180p.
- Goldshtein, M.I.; Litvinov, V.S.; Bronfin, M.F. *Metallophysics of High-Strength Alloys*; Metallurgia: Moscow, Russia, 1986; 312p.
- Materials Parl. *Nickel, Cobalt, and Their Alloys. ASM Speciality Handbook*; materials Parl; ASM International: Novelty, OH, USA, 2000; 400p.
- Bruckart, W.L.; Jaffee, R.I. Cladding of molybdenum for service in air at elevated temperature. *Trans. Am. Soc. Met.* **1952**, *44*, 44.
- Lurie, S.; Volkov-Bogorodskiy, D.; Solyaev, Y.; Rizahanov, R.; Agureev, L. Multiscale modelling of aluminium-based metal-matrix composites with oxide nanoinclusions. *Comput. Mater. Sci.* **2016**, *116*, 62–73. [[CrossRef](#)]
- Kostikov, V.I.; Agureev, L.E.; Ereemeeva, Z.V. Development of nanoparticle-reinforced alumocomposites for rocket-space engineering. *Russ. J. Non Ferr. Met.* **2015**, *56*, 325–328. [[CrossRef](#)]
- Sharma, A.; Roh, M.-H.; Jung, D.-H.; Jung, J.-P. Effect of ZrO₂ Nanoparticles on the Microstructure of Al-Si-Cu Filler for Low-Temperature Al Brazing Applications. *Met. Mater. Trans. A* **2016**, *47A*, 510–521. [[CrossRef](#)]
- Chuvil’deev, V.N.; Kopylov, V.I.; Zeiger, W. A theory of non-equilibrium grain boundaries and its applications to nano- and micro-crystalline materials processed by ECAP. *Ann. Chim. Sci. Des. Matériaux* **2002**, *27*, 55–64. [[CrossRef](#)]
- Ohji, T.; Hirano, T.; Nakahira, A.; Niihara, K. Particle/Matrix interface and its role in creep inhibition in alumina silicon carbide nanocomposites. *J. Am. Ceram. Soc.* **1996**, *79*, 33–45. [[CrossRef](#)]
- Grigorovich, V.K.; Sheftel’, E.N. *Dispersion Hardening of Refractory Metals*; Nauka: Moscow, Russia, 1980; 304p.
- Gottstein, G. *Physical Foundations of materials Science*; Springer: Berlin, Germany, 2004; 502p.
- Thompson, A.W. Substructure strengthening mechanisms. *Met. Trans.* **1977**, *8A*, 833–842. [[CrossRef](#)]
- Lugovskoi, Y.F. Effect of structure on the fatigue strength of dispersion-hardened condensated based on copper II. Analysis of the first coefficient of the Mott—Stroh relation. *Powder Met. Met. Ceram.* **1998**, *37*, 432–437. [[CrossRef](#)]
- Taira, S.; Otani, R. *Theory of High Temperature Strength of materials*; Metallurgiya: Moscow, Russia, 1986; 280p.
- Springer Nature. *Spark Plasma Sintering of materials. Advances in Processing and Applications*; Springer Nature: Cham, Switzerland, 2019; 767p.
- Borkar, T.; Banerjee, R. Influence of spark plasma sintering (SPS) processing parameters on microstructure and mechanical properties of nickel. *Mater. Sci. Eng. A* **2014**, *618*, 176–181. [[CrossRef](#)]
- Zhao, Y.; Topping, T.; Bingert, J.F.; Thornton, J.; Dangelewicz, A.; Li, Y.; Liu, W.; Zhu, Y.; Zhou, Y.; Lavernia, E. High Tensile Ductility and Strength in Bulk Nanostructured Nickel. *Adv. Mater.* **2008**, *20*, 3028–3033. [[CrossRef](#)]

18. Naimi, F.; Minier, L.; Le Gallet, S.; Couque, H.; Bernard, F. Dense Nanostructured Nickel Produced by SPS from Mechanically Activated Powders: Enhancement of Mechanical Properties. *J. Nanomater.* **2013**, *11*. [[CrossRef](#)]
19. Agureev, L.E.; Kostikov, V.I.; Yeremeyeva, Z.V.; Barmin, A.A.; Rizakhanov, R.N.; Ivanov, B.S.; Ashmarin, A.A.; Laptev, I.N.; Rudshiteyn, R.I. Powder aluminum composites of Al–Cu system with micro-additions of oxide nanoparticles. *Inorg. Mater. Appl. Res.* **2016**, *7*, 507–510. [[CrossRef](#)]
20. Mironov, V.V.; Agureev, L.E.; Eremeeva, Z.V.; Kostikov, V.I. Effect of Small Additions of Alumina Nanoparticles on the Strength Characteristics of an Aluminum material. *Dokl. Phys. Chem.* **2018**, *481*, 110–113. [[CrossRef](#)]
21. Lurie, S.; Belov, P.; Volkov-Bogorodsky, D.; Tuchkova, N. Interphase layer theory and application in the mechanics of composite materials. *J. Mat. Sci.* **2006**, *41*, 6693–6707. [[CrossRef](#)]
22. Saunders, Z.; Noack, C.W.; Dzombak, D.A.; Lowry, G. Characterization of engineered alumina nanofibers and their colloidal properties in water. *J. Nanoparticle Res.* **2015**, *17*, 1–14. [[CrossRef](#)]
23. Bravaya, N.M.; Galiullin, A.N.; Saratovskikh, S.L.; Panin, A.; Faingold, E.; Vasilev, S.G.; Bubnova, M.; Volkov, V. Synthesis and properties of hybrid materials obtained by in situ copolymerization of ethylene and propylene in the presence of Al₂O₃ nanofibers (NAFEN™) on catalytic system rac-Et (2-MeInd) 2ZrMe₂/isobutylalumoxane. *J. Appl. Polym. Sci.* **2016**. [[CrossRef](#)]
24. Panda, P.K.; Ramakrishna, S. Electrospinning of Alumina Nanofibers Using Different Precursors. *J. Mater. Sci.* **2007**, *42*, 2189–2193. [[CrossRef](#)]
25. Yang, C.; Huang, H.-F.; de los Reyes, M.; Yan, L.; Zhou, X.-T.; Xia, T.; Zhang, D.-L. Microstructures and Tensile Properties of Ultrafine Grained Ni- (1-3.5) wt.% SiCNP Composites Prepared by a Powder Metallurgy Route. *Acta Met. Sin.* **2015**, *28*, 809–816. [[CrossRef](#)]
26. Maweja, K.; Phasha, M.; Yamabe-Mitarai, Y. Alloying and microstructural changes in platinum–titanium milled and annealed powders. *J. Alloy. Compd.* **2012**, *523*, 167–175. [[CrossRef](#)]
27. Rosenberg, S.J. *Nickel and Its Alloys*; National Bureau of Standards Monograph: Washington, DC, USA, 1968; 106p.
28. Farraro, R.; McLellan, R.B. Temperature dependence of the Young's modulus and shear modulus of pure nickel, platinum, and molybdenum. *Metall. Trans. A* **1977**, *8*, 1563–1565. [[CrossRef](#)]
29. *Engineering Properties of Nickel 200 and 201, Technical Bulletin T-15*; Huntington Alloy Products Division, The International Nickel Co. Inc.: Washington, DC, USA, 1964.
30. *Nickel. Circular of the Bureau of Standarts. No. 100*; Washington Government Printing Office: Washington, DC, USA, 1921; 105p.
31. Bollmann, W. Electron-microscopic observations on the recrystallization of nickel. *J. Inst. Met.* **1959**, *87*, 439.
32. Masatake, Y.; Motoyuki, S.; Hideo, K. Energetics of segregation and embrittling potency for non-transition elements in the Ni Σ5 (012) symmetrical tilt grain boundary: A first-principles study. *J. Phys. Condens. Matter.* **2004**, *16*, 3933. [[CrossRef](#)]
33. Sanyal, S.; Waghmare, U.V.; Subramanian, P.R.; Gigliotti, M.F.X. Effect of dopants on grain boundary decohesion of Ni: A first-principles study. *Appl. Phys. Lett.* **2008**, *93*. [[CrossRef](#)]
34. Young, G.; Najafabadi, R. *Applications of Ab Initio Modeling to materials Science: Grain Boundary Cohesion and Solid State Diffusion*; No. LM-04K037; Lockheed Martin Corporation: New York, NY, USA, 2004.
35. Hanlon, T.; Kwon, Y.-N.; Suresh, S. Grain size effects on the fatigue response of nanocrystalline metals. *Scripta Mater.* **2003**, *49*, 675–680. [[CrossRef](#)]
36. Ragulya, A.V.; Skorokhod, V.V. *Consolidated Nanostructured materials*; Naukova dumka: Kiev, Ukraine, 2007; 369p.
37. Ramakrishnan, P.; Tendolkar, G.S. Influence of thin oxide films on the mechanical properties of sintered metal-powder compacts. *Powder Metall.* **1964**, *7*, 34–49. [[CrossRef](#)]
38. Bhattacharjee, P.P.; Sinha, S.K.; Upadhyaya, A. Effect of sintering temperature on grain boundary character distribution in pure nickel. *Scr. Mater.* **2007**, *56*, 13–16. [[CrossRef](#)]
39. Minier, L.; Le Gallet, S.; Grin, J.; Bernard, F. A comparative study of nickel and alumina using spark plasma sintering (SPS). *Mater. Chem. Phys.* **2012**, *134*, 243–253. [[CrossRef](#)]
40. Takagi, H.; Nishiyama, Y.; Sakamaki, K.; Yoshida, K. Microstructure and Hardness of Ni-NiO Composites Prepared by Powder Metallurgy. *Trans. Jpn. Soc. Mech. Eng. Ser. A* **1995**, *6*, 1933–1939. [[CrossRef](#)]
41. Fujimura, T.; Tanaka, S.-I. In-situ high temperature X-ray diffraction study of Ni/Al₂O₃ interface reactions. *Acta Mater.* **1997**, *45*, 4917–4921. [[CrossRef](#)]
42. Voicu, C.; Popa, F.; Marinca, T.F.; Neamtu, B.V.; Lostun, M.; Lupu, N.; Chicinas, I. Synthesis and characterisation of Al₂O₃/Ni-type composites obtained by spark plasma sintering. *Powder Metall.* **2018**. [[CrossRef](#)]
43. Xie, G.; Ohashi, O.; Song, M.; Furuya, K.; Noda, T. Behavior of oxide film at the interface between particles in sintered Al powders by pulse electric-current sintering. *Metall. Mater. Trans. A* **2003**, *34A*, 699–703. [[CrossRef](#)]
44. Nagae, T.; Yokota, M.; Nose, M.; Tomida, S.; Kamiya, T.; Saji, S. Effects of pulse current on an aluminum powder oxide layer during pulse current pressure sintering. *Mater. Trans.* **2002**, *43*, 1390–1397. [[CrossRef](#)]
45. Dagan, G.; Shen, W.-M.; Tomkiewicz, M. Passivation of Permalloy Thin Films: II. In Situ Characterization of the Oxide Layer by Photoelectrochemical and Impedance Measurements. *J. Electrochem. Soc.* **1992**, *139*, 1855–1861. [[CrossRef](#)]